Kobe University Repository : Kernel

PDF issue: 2026-11-11

Hydrothermal preparation of blue molybdenum bronze nanoribbons: structural changes in mother crystals, related to solid-state conversion and crystallite splitting to…

Nishida, Takamasa

Eda, Kazuo

(Citation)
Journal of Nanoparticle Research,20(2):27-27

(Issue Date)
2018-02

(Resource Type)
journal article

(Version)
Accepted Manuscript

(Rights)
© Springer Science+Business Media B.V., part of Springer Nature 2018. This is a post-peer-review, pre-copyedit version of an article published in Journal of Nanoparticle Research. The final authenticated version is available online at: http://dx.doi.org/10.1007/s11051-018-4134-5

(URL)
https://hdl.handle.net/20.500.14094/90004655

KOBE UNIVERSITY

Hydrothermal Preparation of Blue Molybdenum Bronze Nanoribbons: Structural Changes in Mother Crystals, related to Solid-State Conversion and Crystallite Splitting to Nano-morphology

Takamasa Nishida and Kazuo Eda*

Department of Chemistry, Graduate School of Science, Kobe University,
Rokko-dai 1-1, Nada, Kobe 657-8501, Japan

Corresponding Author

* E-mail: eda@kobe-u.ac.jp. Phone and Fax: +78-803-5677.

Keywords: Blue molybdenum bronze, $A_{0.3}MoO_3$, nanoribbon, nanoparticles, hydrothermal synthesis, solid-state conversion

Abstract

Hydrothermal syntheses of alkali-metal blue molybdenum bronzes nanoribbons, which are expected to exhibit unique properties induced by a combined effect of extrinsic and intrinsic low-dimensionalities, from hydrated-alkali-metal molybdenum bronzes were investigated. Nanoribbons grown along the quasi-one-dimensional (1D) conductive direction of $Cs_{0.3}MoO_3$, which is difficult to prepare by the conventional methods, were first synthesized. The nano-morphology formation is achieved by a solid-state conversion (or crystallite splitting) and subsequent crystallite growth, and the structural changes of the starting material related to the conversion were first observed by powder X-ray diffraction and scanning transmission electron microscopy as a result of finely tuned reaction system and preparation conditions. The structural changes were analyzed by model simulations, and were attributed to the structural modulations that were concerned with the intralayer packing disorder and with two dimensional long range ordered structure, formed in MoO_3 sheets of the hydrated molybdenum bronze. Moreover, the modulations were related to displacement defects of the Mo-O framework units generated

along the [100] direction in the hydrated molybdenum bronze. Then it was suggested that the solid-state conversion into blue molybdenum bronze and the crystallite splitting to nano-morphology were initiated by the breaking of the Mo-O-Mo bonds at the defects.

Introduction

Morphologically low-dimensional or partially nanosized materials have attracted much interest of researchers because of their extraordinary potential for applications. For example, single crystalline materials having low-dimensional morphology such as nanowire, nanoribbon and nanobelt enable effective electronic transportation and supply a large contact area to surrounding environments. Thus various oxides such as MoO_3, $LiMn_2O_4$ and Co_3O_4 have been fabricated as low-dimensional crystals and have been used as conductors and/or active materials for high performance lithium ion batteries, gas sensors and so on (e.g., Nam et al. 2006; Hosono et al.2009; Lupan et al. 2014).

As a further attractive target we are interested in morphologically low-dimensional materials having intrinsically low-dimensional property. A candidate of such materials is a nanoribbon or a nanowire of charge density wave (CDW) materials such as $NbSe_3$, TaS_3, and alkali-metal blue molybdenum bronzes $A_{0.3}MoO_3$ (A-BMBs, A = K, Rb, Cs). Generally CDW materials have quasi-one-dimensional (1D) conductivity at room temperature and exhibit the

Peierls transition into a CDW state at a lower temperature. Owing to the CDW motion, they exhibit numerous interesting behaviors such as nonlinear conductivity (Dumas et al. 1983), memory effect (Fleming and Schneemeyer 1983) and photoresponse (Ogawa et al. 2001). Moreover, they are expected to exhibit unique properties induced by a combined effect of the two kinds of (extrinsic and intrinsic) low-dimensionalities because their electronic behaviors vary depending on interactions among conductive chains that concern the quasi-1D conduction (Grüner 1994). Indeed, nanowire-like particles of $NbSe_3$ and TaS_3 have been prepared and investigated to analyze unique electronic characteristics such as the Luttinger-liquid-like behavior (van der Zant et al. 2001; Slot et al. 2001; Zaitsev-Zotov 2003; Slot et al. 2004).

A-BMBs show large CDW responses and are known as the CDW materials in which sliding CDW was first observed (Dumas et al. 1983). They have a layer structure consisting of infinite MoO_3 sheets connected by *A* cations located at intersheet positions as shown in Figure 1 (Graham and Wadsley 1966). Thus their interchain interactions and impurity properties can be modified by the kind and the amount of *A* cations without changing the structure of the

conductive chains (i.e. 1D conduction path), unlike $NbSe_3$ and TaS_3. Therefore, preparations of their nanoribbons are useful for fundamental understanding of the behaviors of the CDW materials in terms of the interchain interactions and consequently for developing materials having unique properties. However, while $NbSe_3$ and TaS_3 are prepared by the chemical vapor transport method (Borodin et al. 1987; Slot 2005), *A*-BMBs cannot be prepared by the method and their nanoribbons are, thus, difficult to prepare. Furthermore, Cs-BMB, which has the largest separation between the adjacent conductive chains in a series of *A*-BMBs, is more difficult to prepare because of the existence of another stable phase which competes with formation of Cs-BMB, unlike the other *A*-BMBs (Reid and Watts 1970; Mumme and Watts 1970; Collins et al. 1988). Thus, even its presence has not been almost recognized by materials researchers, although only we succeeded in preparing its powdered specimen (Eda et al. 1998, 2005a).

So far we have studied various preparation methods of *A*-BMBs. In one of the studies we succeeded in preparing single phase of K-BMB by hydrothermal treatments of hydrogen molybdenum bronze H_xMoO_3 (HMB) with the KCl solution in an oxygen-free autoclave, and found that K-BMB was formed as

needle-shaped small crystallites by exfoliation from the surface of the mother HMB crystal (i.e., "crystallite splitting", which leads to nano-morphology formation), as shown in Figure 2 (Chin et al. 2002; Eda et al. 2005b). Therefore, we suggested that the formation of the K-BMB crystallites proceeded via a solid-state conversion [from HMB through an intermediate, hydrated-alkali-metal molybdenum bronze (Hyd-*A*-MB), which is an ion exchange product of HMB with A^+, to K-BMB], although we could not obtain further information for understanding a detailed conversion mechanism because of complexity in the reaction system (coexistence of starting and intermediate materials during the conversion to K-BMB). Furthermore, to make tuning of preparation conditions (strictly speaking, operations for the preparation) easier we recently improved the hydrothermal method to be feasible with a non-oxygen-free autoclave by using alcohols as an oxygen scavenger (Nishida et al. 2013). Then, we fully tuned its preparation conditions for subsequent elongation of the K-BMB crystallites to achieve the single phase preparation of K-BMB nanoribbons in a one-pot procedure. However, because of the complexity in the reaction system and the competition of the conversion

process with a decomposition process of HMB under hydrothermal conditions (Eda et al. 2005b) we have not achieved the clarification of the detailed conversion mechanism and the preparation of Cs-BMB nanoribbons.

In this study, to make the reaction system simpler we have examined a direct preparation of *A*-BMB from Hyd-*A*-MB, which is an intermediate in the previous preparation method. Then, we first succeeded in preparing Cs-BMB nanoribbons, and found interesting structural changes of the starting material that concern the solid-state conversion and the crystallite splitting to nano-morphology. The structural changes were discussed on the basis of model simulations to understand the detailed mechanism of the solid-state conversion.

Materials and Methods

Starting materials

Hyd-*A*-MB was prepared by ion exchange from Hyd-Na-MB which was obtained by the method of Thomas and McCarron (Thomas and McCarron 1986). The prepared Hyd-*A*-MBs were filtrated and washed with distilled water.

Hydrothermal procedure

In a typical hydrothermal procedure, 100 mg of the starting material was suspended in 15 mL hydrothermal solvent (0.5 M KCl or 0.1 M CsCl solution with 0.01 M HCl and 1 v/v % ethanol). The resulting suspension was put into a 28 mL Teflon-lined autoclave and heated at 453 K for the desired time.

Measurements

Powder X-ray diffraction (XRD) of the samples were measured by using a Rigaku SmartLab diffractometer with Cu-Kα radiation (40 KV, 30 mA). Scanning electron microscopy (SEM) was carried out with a JSM-5610LVS (JEOL). Transmission electron microscopy (TEM) and scanning transmission electron microscopy (STEM) were carried out with JEM-2010 and JEOL 2100F respectively. The contents of the alkali-metal and molybdenum in the samples were determined by using a Hitachi Z-2010 atomic absorption spectrometer and the content of Mo^{5+} in the samples was determined by the method of Choain and Marion (chemical titration analysis) (Choain and Marion 1963).

Results and discussion

Hydrothermal synthesis of *A*-BMB from Hyd-*A*-MB

Starting material Hyd-K-MB and Hyd-Cs-MB. So-called vacuum-dried Hyd-Cs-MB having a typical composition of $[Cs\cdot(H_2O)_{0.31}]_{0.22}H_{0.01}MoO_3$ (Eda et al. 1998) was prepared, and used as a starting material for the present hydrothermal syntheses. On the other hand, so-called vacuum-dried Hyd-K-MB could not be prepared, though tried several times. Figure 3a shows a typical XRD pattern of Hyd-K-MB prepared in the present study. It was slightly different from the pattern (Figure 3b) calculated from the crystal structure of the vacuum-dried Hyd-K-MB (a=3.729, b=21.55, c=3.828 Å, space group: *Cmmm*, Figure 4a) (Sotani et al. 1997). According to our analysis based on computer simulation of the diffraction pattern, the newly obtained Hyd-K-MB has a different type of stacking pattern of the MoO_3 sheets and has a slightly wider gap between adjacent sheets (the structure is shown in Figure 4b). The XRD pattern calculated from the new structural model agreed well with the observed one (Figures 3a and 3c). This type of Hyd-K-MB (a=3.724, b=22.14, c=3.931 Å, space group: $Pna2_1$) was used as a starting material for the hydrothermal syntheses. Its typical composition was $(K\cdot nH_2O)_{0.25}H_{0.10}MoO_3$,

n=ca. 4.

Synthesis of K-BMB. We performed hydrothermal synthesis of K-BMB from Hyd-K-MB. After tuning its preparation conditions (some examples are shown in Figures S1 and S2) we succeeded in preparing a single phase of K-BMB nanoribbons. Figure 5 shows the XRD pattern of the resulting K-BMB, obtained by the hydrothermal treatment ([KCl]=0.5 M, [HCl]=0.01 M, [ethanol]=1.0 v/v%) at 453 K for 36 hours, together with the pattern calculated from the crystal data of K-BMB (ICSD-14350). The positions of the peaks in the two diffraction patterns fully agreed with each other, supporting the formation of single phase of K-BMB. Figure S3 shows SEM images of the obtained K-BMB nanoribbons. The K-BMB nanoribbons precipitated as scrubbing-bush-like aggregates. Individual nanoribbons had a size of over 50 μm in length and ca. 100-200 nm in width. Figure 6 shows a TEM image and a selected area electron diffraction (SAED) pattern of an isolated nanoribbon. The SAED pattern was indexed to the **[104]** zone axis of monoclinic K-BMB. On the basis of these results, it is demonstrated that the nanoribbon was a single crystal of K-BMB and was well grown along the crystal *b* axis similarly as the nanoribbons

obtained from HMB (Nishida et al. 2013). According to the atomic absorption and chemical titration analyses, the composition of the nanoribbon was $K_{0.29}MoO_3$.

Synthesis of Cs-BMB. We examined hydrothermal synthesis of Cs-BMB nanoribbons from Hyd-Cs-MB. After tuning its preparation conditions, though as a part of a mixture, we first succeeded in preparing Cs-BMB nanoribbons by the hydrothermal treatment at 453 K for 36 hours ([CsCl]=0.1 M, [HCl]=0.01 M, [ethanol]=1.0 v/v%). The SEM observation of the product confirmed the formation of nanoribbons (Figure 7). The size of individual nanoribbons was about the same as that of K-BMB nanoribbons mentioned above. Figure 8 shows a TEM image and a SAED pattern of the product. The observed SAED pattern was indexed to **[104]** zone axis of monoclinic Cs-BMB, supporting the formation of Cs-BMB nanoribbons. According to the results, the obtained Cs-BMB nanoribbons were also well grown along the crystal *b* axis. Moreover, although its precise composition could not be determined by the atomic absorption and chemical titration analyses because of a mixture, the energy dispersive X-ray spectrometry (EDX) analysis (Figure S4) showed that the composition of the

nanoribbon was $Cs_{0.26}MoO_{2.88}$ and agreed roughly with the ideal composition of $Cs_{0.3}MoO_3$.

Conversion processes of Hyd-*A*-MB to *A*-BMB under the hydrothermal conditions

To reveal the detailed mechanism of the solid-state conversion we investigated the formation process of K-BMB from Hyd-K-MB. Figure 9 shows XRD patterns of the products obtained at various treatment times. According to the results, contrasted changes in intensity of the peaks occurred depending on the diffraction indices in the XRD pattern of Hyd-K-MB before turning into K-BMB. That is, only a few specific peaks, indexed to 1 3 0, 1 5 0, and 1 2 1 reflections, drastically decreased their intensities and broadened their widths depending on the treatment time. Moreover, all the peaks observed exhibited slight shifts of their positions, and thus the lattice constants also slightly changed, as shown below. These changes were irreversible and were necessarily observed just before the conversion to K-BMB. Thus, the changes were supposed to be necessary for the solid-state conversion. According to the SEM investigation the morphology of the Hyd-K-MB particles exhibits little remarkable changes until 18 hours of the hydrothermal treatment (Figures S5a–S5c). After the hydrothermal treatment for 21 hours, some splitting traces were observed on the Hyd-K-MB particles (Figure S5d), supporting the solid-state formation of

K-BMB by the crystallite splitting. However, there were no remarkable changes in the XRD pattern between the products obtained by the treatments for 18 and 21 hours (Figures 9c and S6), because the content of K-BMB is still very small in the latter product. After more than 21 hours of the treatments, the BMB crystals grow rapidly (Figures S5e and S5f). In the case of the preparation condition used in the present study the K-BMB crystals grow into the nanoribbons, once its nuclei were formed (see Figure 2 of Nishida et al. 2013).

To reveal the origin of the changes of Hyd-K-MB observed in Figure 9 we performed computer simulations of the XRD patterns based on several structure models and found that their drastic intensity changes of the specific peaks were attributed to an intralayer packing disorder of MoO_3 sheets. In the disordered structure original units of Hyd-K-MB (Figure 10a) and units antiphased by the atomic position shift of $a/2$ along the **[100]** direction (Figure 10b) are randomly located, and the lattice constants were a=3.783, b=22.25, c=3.892 Å (space group: $Pna2_1$). The structural models (Figures 10c–10e) reproduced well the intensity changes of the specific XRD peaks and the peak shifts of individual peaks, observed in Figures 9a–9c (see Figures 10f–10h). However, since direct contact of the antiphase unit to the original unit is not permitted because of avoiding abnormal atomic distances, we suppose that a real intralayer packing disorder is formed by displacement defects of the Mo-O framework units, shown in Figure S7. Although the Rietveld analysis was

expected to be applicable for the confirmation of the model, the intermediate products were not homogeneous enough for the analysis.

Then we further investigated the defect structure by STEM. Figure 11 shows a TEM mode image and a SAED pattern of the product obtained by the hydrothermal treatment at 453 K for 6h. The observed SAED pattern was indexed to the **[010]** zone axis of the orthorhombic structure of Hyd-K-MB. As shown in Figure 11b, several spots such as 1 0 0 reflection (indicated by a circle in the figure) split in two directions; clearly (with a clear split width) in the **[001]*** reciprocal direction and diffuse streak-like in the **[100]*** direction. Such splitting of the diffraction spots could be explained in terms of two-dimensional (2D) long range ordered (LRO) structure (Watanabe and Ogawa 1956; Konno et al. 1999) which has superperiods M_x and M_z along the **[100]** and **[001]** directions respectively. The schematic diagram of 2D LRO structure model used in this study is shown in Figure 12, where I is an elementary unit corresponding to the original orthorhombic unit cell (with a size of $a \times b \times c$) of Hyd-K-MB (Sotani et al. 1997) and II, III, IV are antiphased along a certain, another, and the both directions respectively. The exact unit cell of the 2D LRO structure is also

orthorhombic and has a size of $2M_x a \times b \times 2M_z c$. The intensity of reflection at a reciprocal point $h\ 0\ l = q_x\ 0\ q_z$ of this 2D LRO structure is simply given by a following equation.

$$I(q_x,0,q_z) = \left[F^{\mathrm{I}}(q_x,0,q_z) + F^{\mathrm{II}}(q_x,0,q_z)\mathrm{e}^{-2\pi i M_z q_z} + F^{\mathrm{III}}(q_x,0,q_z)\mathrm{e}^{-2\pi i M_x q_x} + F^{\mathrm{IV}}(q_x,0,q_z)e^{-2\pi i M_z q_z}\mathrm{e}^{-2\pi i M_x q_x}\right]^2 \left(\frac{\sin\pi M_x q_x}{\sin\pi q_x}\frac{\sin\pi M_z q_z}{\sin\pi q_z}\right)^2 \left(\frac{\sin\pi N_x{*}2M_x q_x}{\sin\pi 2M_x q_x}\frac{\sin\pi N_z{*}2M_z q_z}{\sin\pi 2M_z q_z}\right)^2$$

eq. 1.

where $F^{\mathrm{I}}(q_x,0,q_z)$, $F^{\mathrm{II}}(q_x,0,q_z)$, $F^{\mathrm{III}}(q_x,0,q_z)$, $F^{\mathrm{IV}}(q_x,0,q_z)$ are interference functions at $q_x,0,q_z$ of the units I, II, III, and IV respectively. N_x and N_z are respectively the numbers of the LRO unit cell along the **[100]** and **[001]** directions in a single LRO crystallite. The first and second terms are respectively the structural factor and the apparent Laue function of the structural unit consisting of I, II, III and IV, and the product of these two terms corresponds to the crystal structural factor of the LRO unit cell. The third term is the Laue function of the LRO crystallite. From the splitting widths (corresponding to a^*/M_x for the **[100]*** direction and c^*/M_z for the **[001]*** direction) observed in Figure 11b, it was evaluated that M_x = 4 and M_z = 6. Since the splitting spots were diffuse along the **[100]*** direction, the existence of structures with various superperiods

along the [100] direction was supposed. Thus, note that $M_x = 4$ was evaluated as the most expectable value. Simultaneously the diffuse streak-like spots along the [100]* direction indicate less periodicity of the LRO structure along the [100] direction (i,e, N_x is smaller than N_z). Thus we conveniently used $N_x = 2$ and $N_z = 4$ for the calculation. Figure 13 shows the profiles of the scattering intensity at q_x 0 0 in the range of $0.5 < q_x < 1.5$ and at 1 0 q_z in the range of $-0.5 < q_z < 0.5$, calculated for the 2D LRO structure. The positions of O, K, and Mo atoms in the units I, II, III and IV used for the calculation are given in Table S1. The 2D LRO model roughly reproduced the splitting (clearly in the [001]* direction and diffuse in the [100]* direction) of the SAED spots observed. Thus we should emphasize that the structure antiphased along the [100] direction in the 2D LRO model is directly related to the displacement defects described above in the discussion for the changes in powder XRD patterns of the Hyd-K-MB hydrothermally treated, while that antiphased along the [001] direction is concerned only with the positional displacement of K atoms (see Table S1). Moreover, according to comparison between the crystal structures of these two compounds, because the crystal *b* axis of *A*-BMB has structural

resemblance to the crystal *c* axis of Hyd-*A*-MB the solid-state (partially topotactic) conversion of Hyd-*A*-MB into *A*-BMB well grown along the crystal *b* axis requires breaking of the Mo-O-Mo bonds formed along the [100] direction and maintaining of the bonds formed along the [001] direction in the Hyd-*A*-MB crystal. Because the defects, mentioned above, weaken the Mo-O-Mo bonds and consequently make breaking of the bonds along the [100] direction easy, it is suggested that the structural modulations found induces the conversion to A-BMB nanoribbons; that is, the conversion is initiated by the accumulation of enough amounts of such defects, supporting the results observed in Figure 9.

Concluding remarks

We succeeded in improving our hydrothermal preparation method of nanoribbons of *A*-BMBs. The improved method especially enables us to prepare nanoribbons of Cs-BMB, which is difficult to prepare and has not been almost recognized even as a family of *A*-BMBs. The resulting nanoribbons are regarded as morphologically low-dimensional materials having intrinsically low-dimensional property, and are expected to become an attractive subject for

study about unique properties induced by a combined effect of extrinsic and intrinsic low-dimensionalities.

Furthermore, to reveal the detailed mechanism of the solid-state conversion to A-BMB and of the crystallite splitting to nano-morphology we investigated the conversion processes. As the results of the simple reaction system selected and of fully tuned preparation conditions, we could observe pure structural changes of the starting material during the conversion. The analysis of the changes by using computer simulation revealed that the intralayer packing disorder and the two dimensional long range ordered structure were formed in the hydrated molybdenum bronze crystal used as a starting material before turning into K-BMB. Then the structural modulations concerned with the intralayer packing disorder and with the long range ordered structure along the [100] direction were related to displacement defects of the Mo-O framework units along the [100] direction. Then it was suggested that the solid-state conversion to the K-BMB crystallites well grown along the 1D conductive direction and the crystallite splitting to nano-morphology were induced by breaking of the Mo-O-Mo bonds at the defects. Since materials

preparations via a solid-state conversion enable us to control the structure of the product by varying the structure of the starting material, searching such solid-state conversions under hydrothermal conditions and analyzing them systematically will provide novel tools useful for material designs and for nano-morphology control. We believe and hope that the present report provides a trigger to draw out a wealth of knowledge on solid-state conversions, accumulated in materials scientists, and to promote the development of such tools.

Acknowledgements

This work was supported by the Grant-in-Aid for Scientific Research (C) No. 23550226 and No. 26410073 of the Ministry of Education, Culture, Sports, Science and Technology of Japan.

Electronic supplementary material: The online version of this article (doi:10.1007/) contains supplementary material, which is available to authorized users.

Conflict of Interest: The authors declare that they have no conflict of interest.

References

Borodin DV, Zaitsev-Zotov SV, Nad FY (1987) Coherence of a charge density wave and phase slip in small samples of a quasi-one-dimensional conductor TaS_3. Journal of Experimental and Theoretical Physics 66:793–802.

Chin K, Eda K, Sotani N, Whittingham MS (2002) Hydrothermal synthesis of the blue potassium molybdenum bronze, $K_{0.28}MoO_3$. Journal of Solid State Chemistry 164:81–87.

Choain C, Marion F (1963) Dosage des oxydes de tungstene et de molybdene. Bulletin de la Société chimique de France 1963: 212.

Collins BT, Ramanujachary KV, Greenblatt M (1988) Preparation and Transport properties of the substituted blue bronze $(Rb_{1-x}Cs_x)_{0.3}MoO_3$. Journal of Solid State Chemistry 77:348–355.

Dumas J, Schlenker C, Marcus J, Buder R (1983) Nonlinear conductivity and noise in the quasi one-dimensional blue bronze $K_{0.30}MoO_3$. Physical Review

Letters 50:757–760.

Eda K, Miyazaki T, Hatayama F, Nakagawa M, Sotani N (1998) Cesium-sodium ion exchange on hydrated molybdenum bronze and formation of new cesium molybdenum bronze by a low-temperature synthesis route. Journal of Solid State Chemistry 137:12–18.

Eda K, Kunotani F, Uchiyama N (2005a) Low-temperature synthetic route based on the amorphous nature of giant species for preparation of lower valence oxides. Journal of Solid State Chemistry 178:1471–1477.

Eda K, Chin K, Sotani N, Whittingham MS (2005b) Hydrothermal synthesis of potassium molybdenum oxide bronzes: structure-inheriting solid-state route to blue bronze and dissolution/deposition route to red bronze. Journal of Solid State Chemistry 178:158–165.

Fleming RM, Schneemeyer LF (1983) Transient electrical response of $K_{0.30}MoO_3$. Physical Review B 28:6996–6999.

Graham J, Wadsley AD (1966) The crystal structure of the blue potassium molybdenum bronze, $K_{0.28}MoO_3$. Acta Crystallographica 20:93–100.

Grüner G (1994) Density Waves in Solids, Addison-Wesley, New York.

Hosono E, Kudo T, Honma I, Matsuda H, Zhou H (2009) Synthesis of single crystalline spinel $LiMn_2O_4$ nanowires for a lithium ion battery with high power density. Nano Letters 9:1045–1051.

Konno TJ, Uehara M, Hirosawa S, Sumiyama K, Suzuki K (1999) Electron diffraction study on the long-range-ordered metastable Fe-Nd-B phase. Philosophical Magazine A 79:2413–2436.

Lupan O, Cretu V, Deng M, Gedamu D, Paulowicz I, Kaps S, Mishra YK, Polonskyi O, Zamponi C, Kienle L, Trofim V, Tiginyanu I, Adelung R (2014) Versatile growth of freestanding orthorhombic α-molybdenum trioxide nano- and microstructures by rapid thermal processing for gas nanosensors. The Journal of Physical Chemistry C 118:15068–15078.

Mumme WG, Watts JA (1970) The crystal structure of the molybdenum bronze Cs_xMoO_3 ($x \approx 0.25$). Journal of Solid State Chemistry 2:16–23.

Nam KT, Kim D-W, Yoo PJ, Chiang C-Y, Meethong N, Hammond PT, Chiang Y-M, Belcher AM (2006) Virus-enabled synthesis and assembly of nanowires for lithium ion battery electrodes. Science 312:885–888.

Nishida T, Eda K, Takahashi K, Sakurai T, Ohta H, Whittingham MS (2013)

Preparation of nanoribbons of blue potassium molybdenum bronze. Chemistry Letters 42:1514–1516.

Ogawa N, Shiraga A, Kondo R, Kagoshima S, Miyano K (2001) Photocontrol of dynamic phase transition in the charge-density wave material $K_{0.3}MoO_3$. Physical Review Letters 87:256401.

Reid AF, Watts JA (1970) Single crystal syntheses by the electrolyses of molten titanates, molybdates and vanadates. Journal of Solid State Chemistry 1:310–318.

Slot E, van der Zant HSJ, Thorne RE (2001) Electric-field distribution near current contacts of anisotropic materials. Physical Review B 65:033403.

Slot E, Holst MA, van der Zant HSJ, Zaitsev-Zotov SV (2004) One-dimensional conduction in charge-density-wave nanowires. Physical Review Letters 93:176602.

Slot E (2005) Microscopic charge density wave transport. Ph.D. thesis, Leiden University.

Sotani N, Suzuki T, Eda K, Yanagi-ishi M, Takagi S, Hatayama F (1997) Preparation of hydrated potassium molybdenum bronzes and their thermal

decomposition. Journal of Solid State Chemistry 132:330–336.

Thomas DM, McCarron EM III (1986) The composition and proposed structure of the alkali metal layered molybdenum bronzes. Materials Research Bulletin 21:945–960.

van der Zant HSJ, Slot E, Zaitsev-Zotov SV, Artemenko SN (2001) Negative resistance and local charge-density-wave dynamics. Physical Review Letters 87:126401.

Watanabe D, Ogawa S (1956) On the superstructure of the ordered alloy Cu_3Pd I. electron diffraction study. Journal of the Physical Society of Japan 11:226-239.

Zaitsev-Zotov SV (2003) Transport properties of TaS_3 and $NbSe_3$ crystals of nanometer-scale transverse dimensions. Microelectronic Engineering 69:549–554.

Figure captions

Figure 1 The crystal structure of *A*-BMB.

Figure 2 Crystallite splitting: a mother crystal during the conversion to K-BMB. Reprinted from J Solid State Chem, 178, Eda K, Chin K, Sotani N, Whittingham MS, Hydrothermal synthesis of potassium molybdenum oxide bronzes: structure-inheriting solid-state route to blue bronze and dissolution/deposition route to red bronze, 158–165, Copyright (2005), with permission from Elsevier.

Figure 3 The XRD pattern of as-prepared Hyd-K-MB (a) and the patterns calculated for the vacuum-dried Hyd-K-MB (*Cmmm*) (b) and the newly found Hyd-K-MB ($Pna2_1$) (c).

Figure 4 The crystal structures of the vacuum-dried Hyd-K-MB (a) and the newly found Hyd-K-MB (b). The occupancy of the K site is 0.5 in the both structures.

Figure 5 The XRD pattern of the product (a) and the pattern calculated from the crystal data of K-BMB (b).

Figure 6 The TEM image (a) and the SAED pattern (b) of the K-BMB

nanoribbon obtained.

Figure 7 The SEM images of the product at low magnification (a) and at high magnification (b).

Figure 8 The TEM image (a) and the SAED pattern (b) of the Cs-BMB nanoribbon.

Figure 9 The XRD patterns of the starting Hyd-KMB (a) and the products obtained by the hydrothermal treatment ([KCl]=0.5 M, [HCl]=0.01 M, [ethanol]=1.0 v/v%) at 453 K for 6 hours (b), 18 hours (c), 24 hours (d) and 36 hours (e). ● and ▲ indicate Hyd-K-MB and K-BMB respectively.

Figure 10 The crystal models and their XRD patterns simulated: an original unit of Hyd-K-MB (a) and its antiphase unit (b). The ratio of unit numbers (a) : (b) in the models are 1:0 for (c) and (f), 3:1 for (d) and (g), 1:1 for (e) and (h), respectively. The occupancy of the K sites is 0.5 in the units.

Figure 11 The TEM image (a) and the SAED pattern (b) of the product obtained.

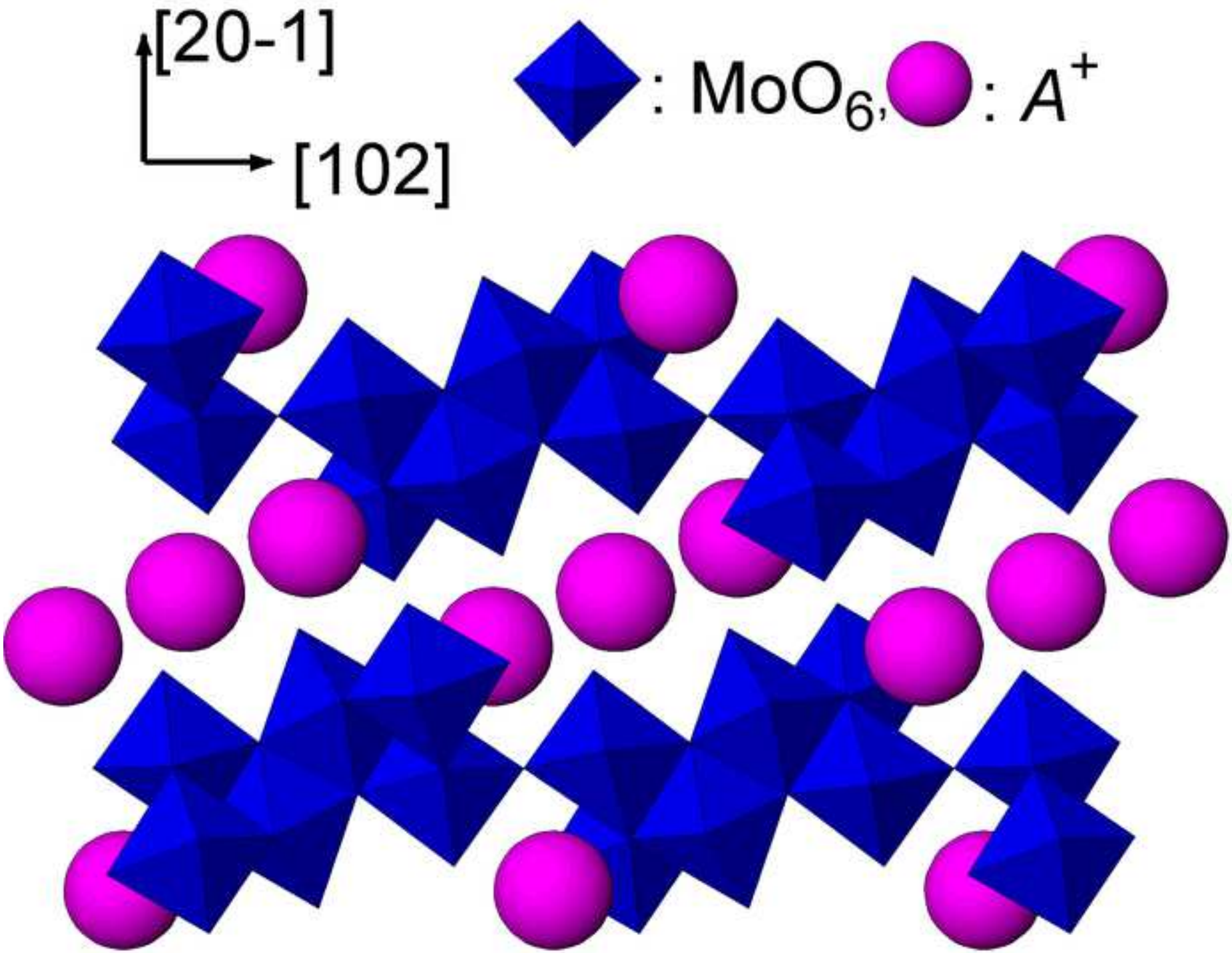
Figure 12 The schematic diagram of the 2D LRO model.

Figure 13 The profiles of scattering intensity at q_x 0 0 ($0.5 < q_x < 1.5$) and 1 0 q_z ($-0.5 < q_z < 0.5$). (a), (e); (b), (f); (c), (g); and (d), (h) respectively show the

profiles of the first term, the second term, the third term, and the total intensity I of eq1.

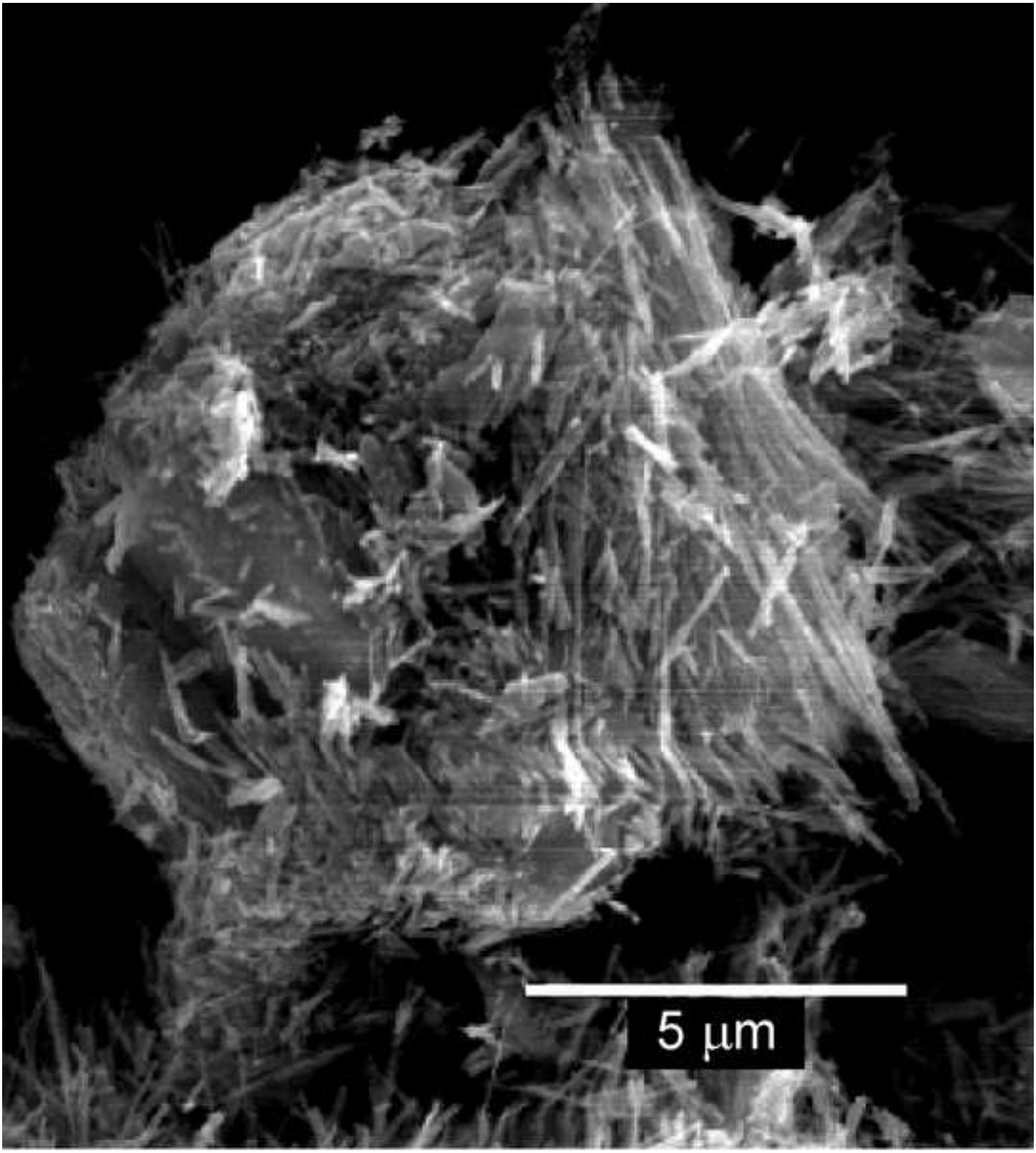
Figure

Click here to download Figure Figure 1 - KBMB.tif



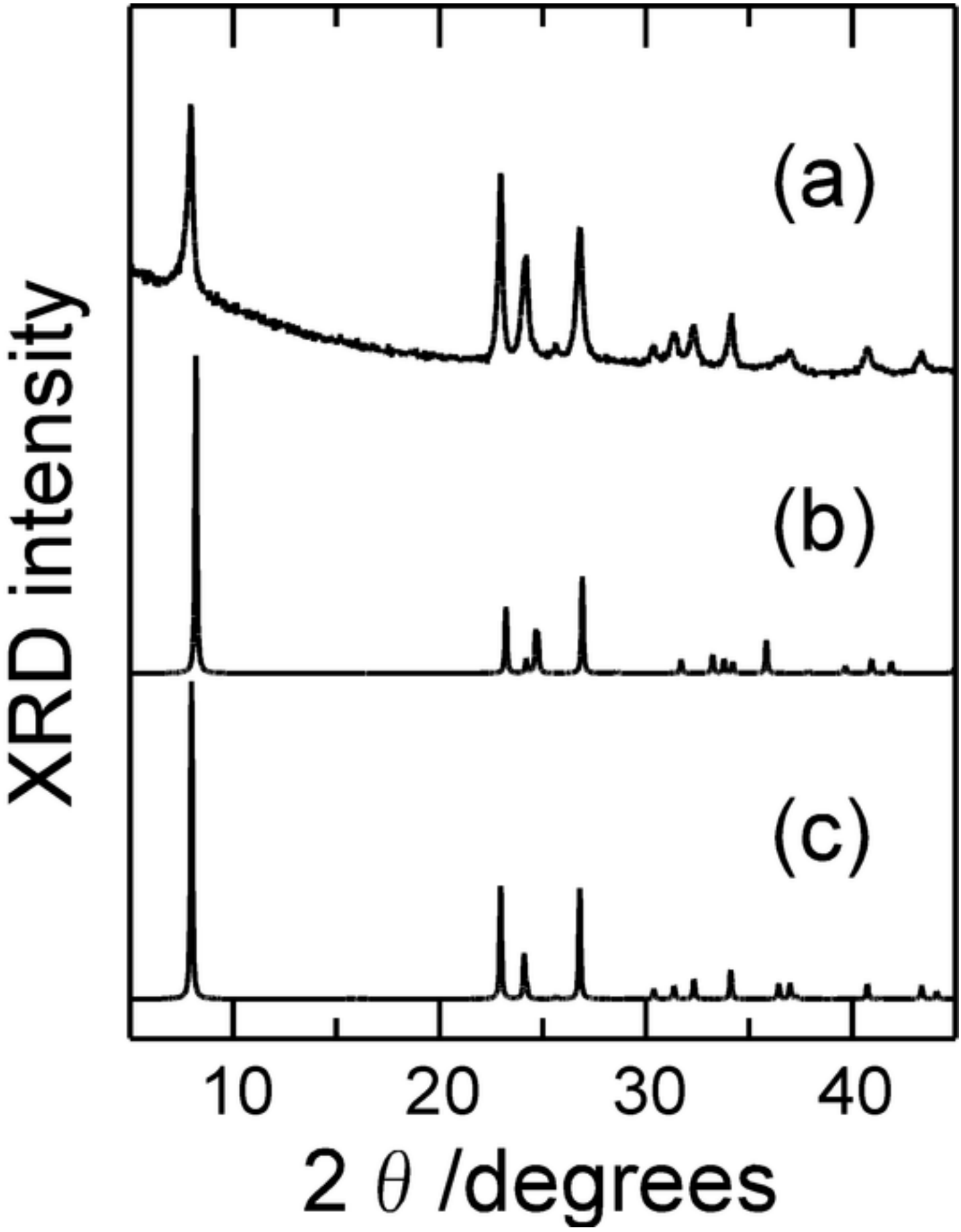
Figure

Click here to download Figure Figure 2_Splitting.tif



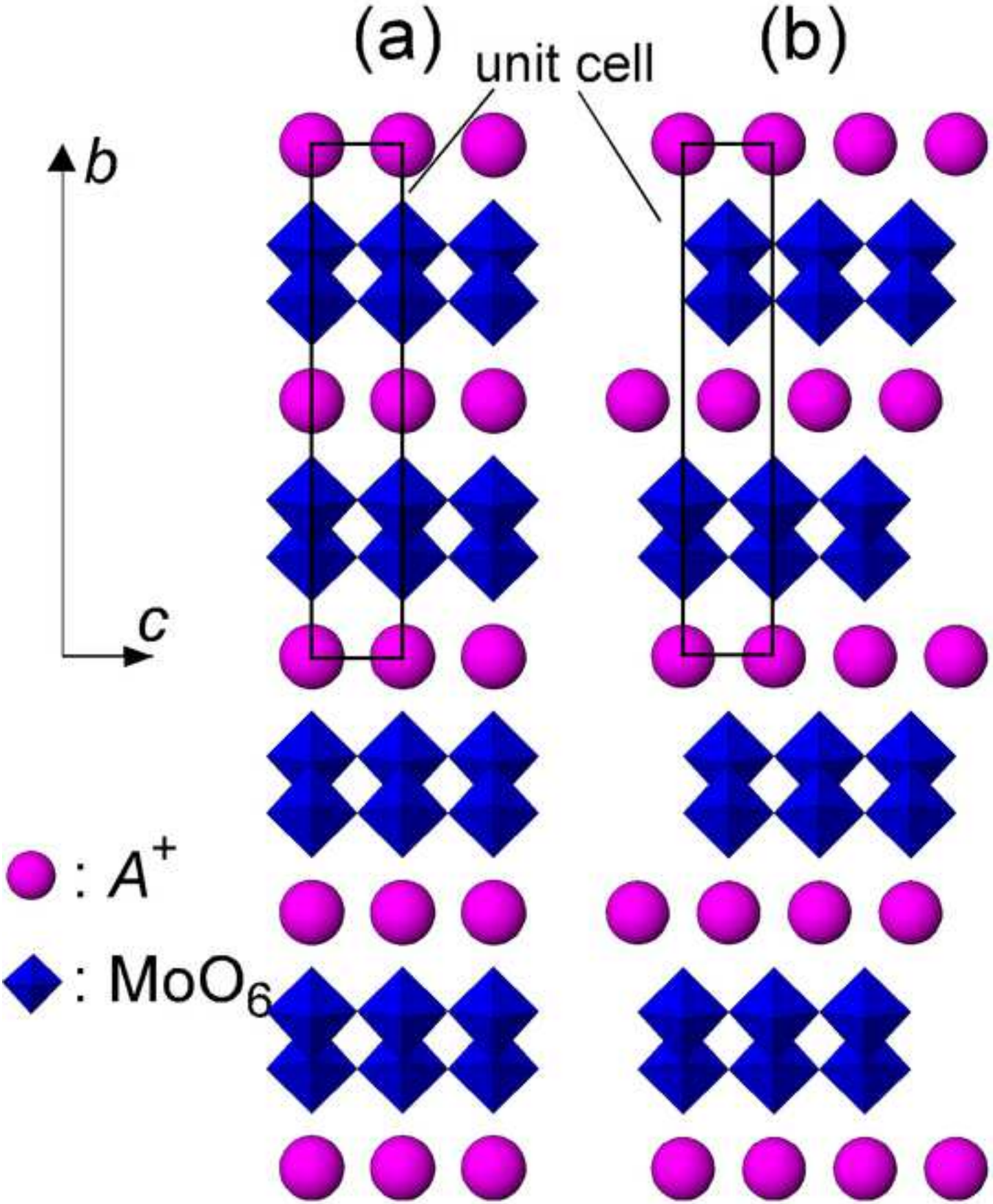
Figure

Click here to download Figure Figure 3 - XRD HydKMB to K BMB 50 x 60 mm.tif



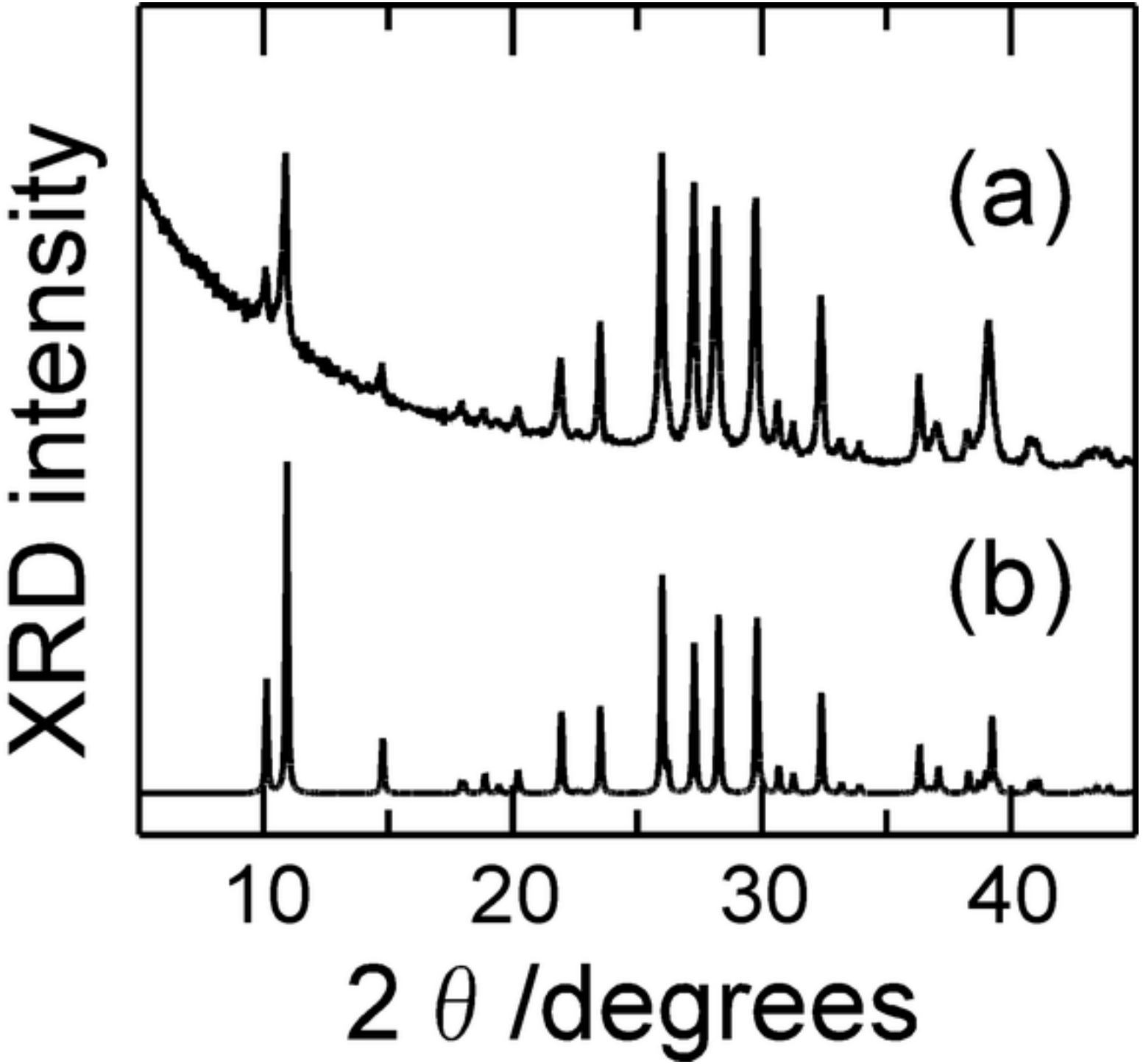
Figure

Click here to download Figure Figure 4 - StructureofStartingHydKB.tif



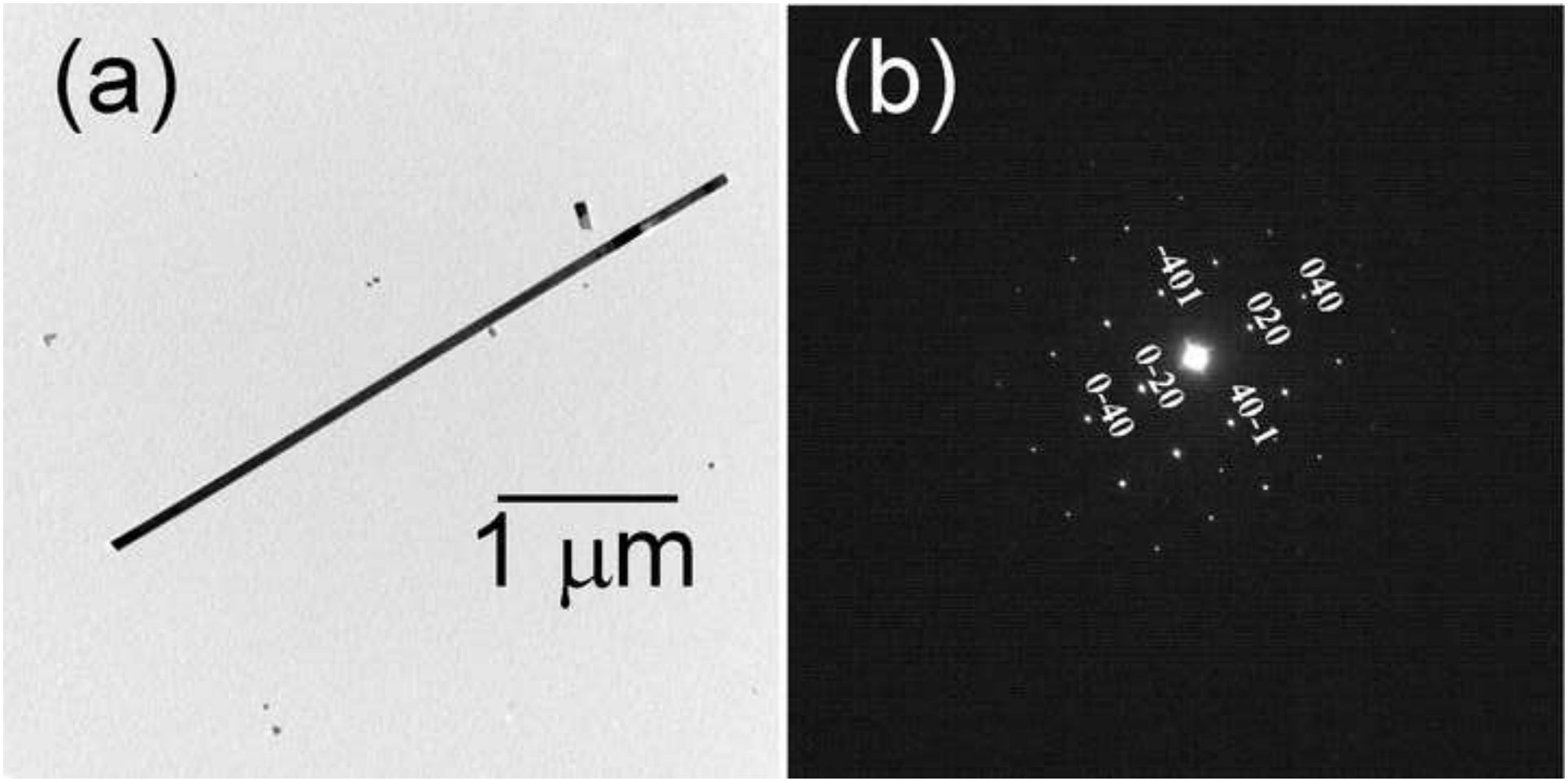
Figure

Click here to download Figure Figure 5 -K BMB 50 x 60 mm.tif



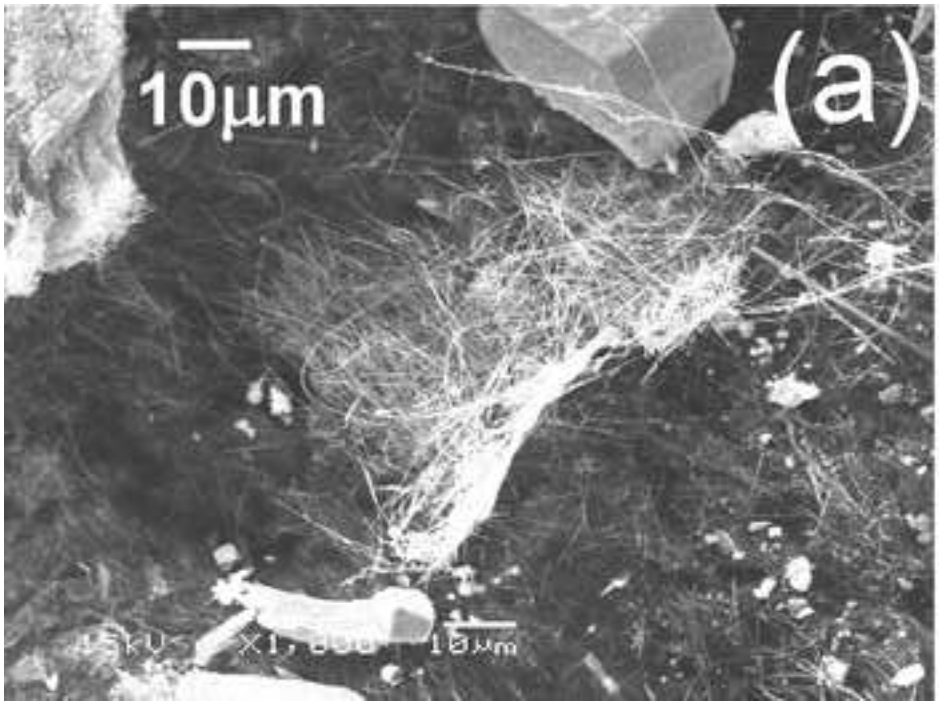
Figure

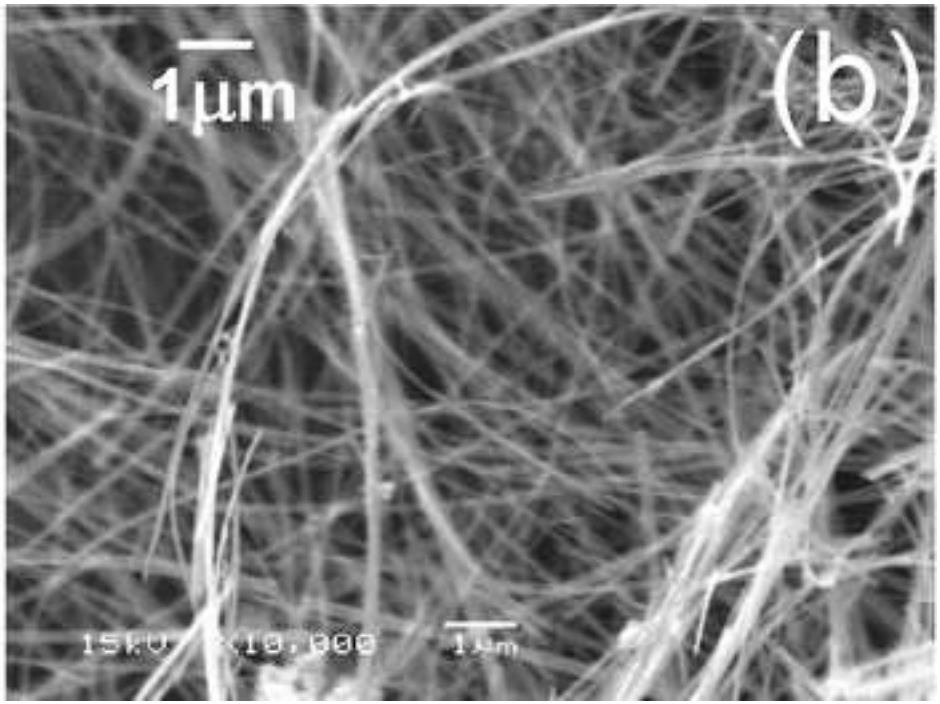
Click here to download Figure Figure 6 - TEM SAED HydKMB to KBMB - 3.tif



Figure

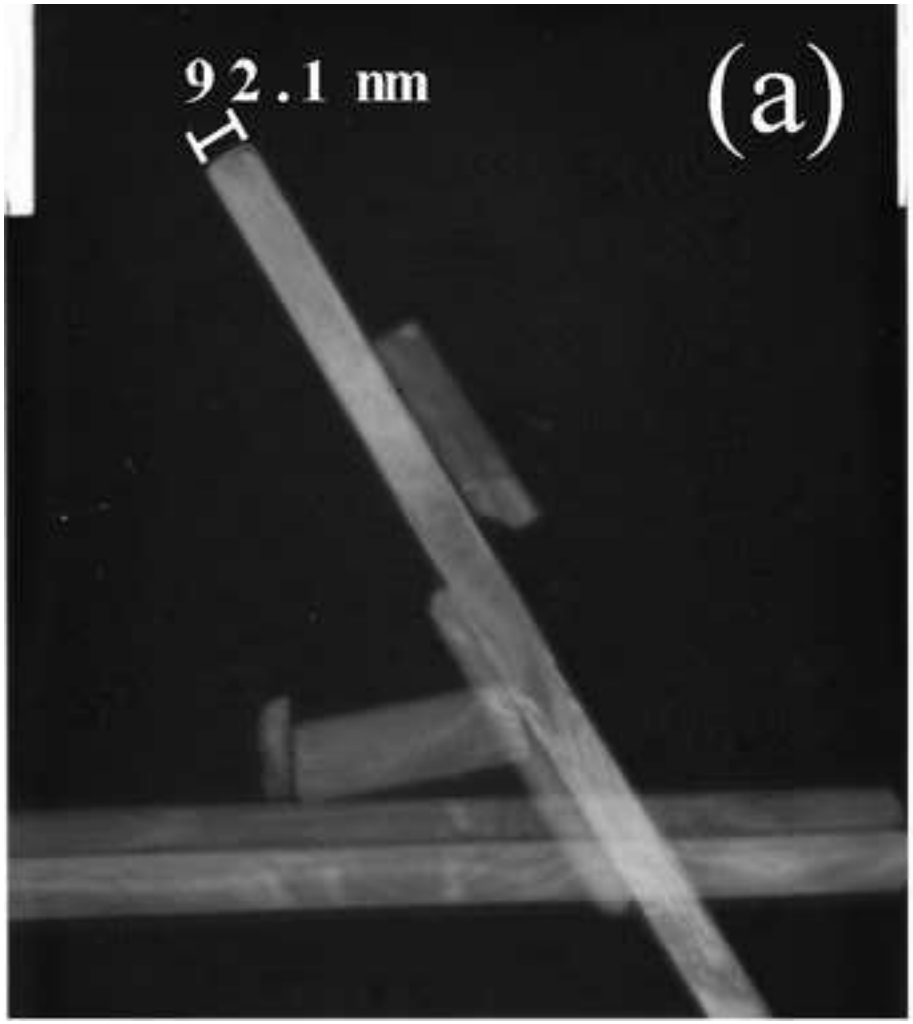
Click here to download Figure Figure 7 - SEM of CsBMB 30 x 82 5 mm 600dpi.tif

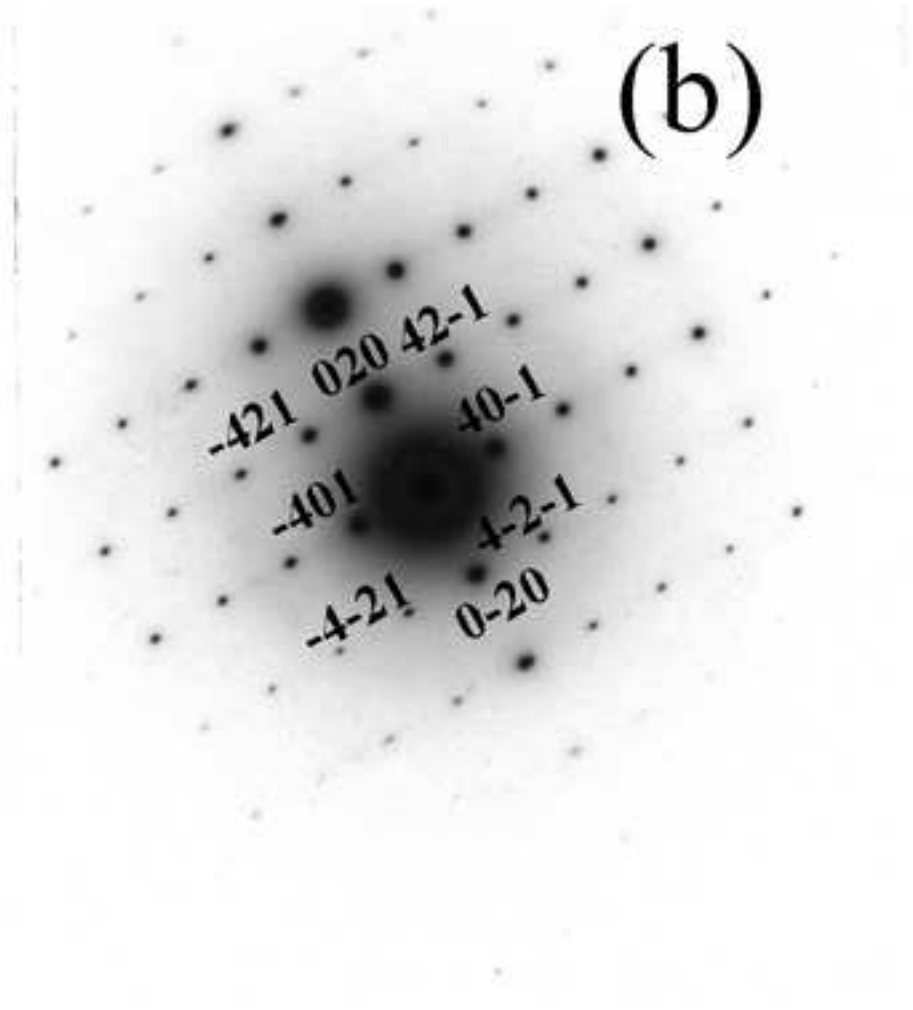




Figure

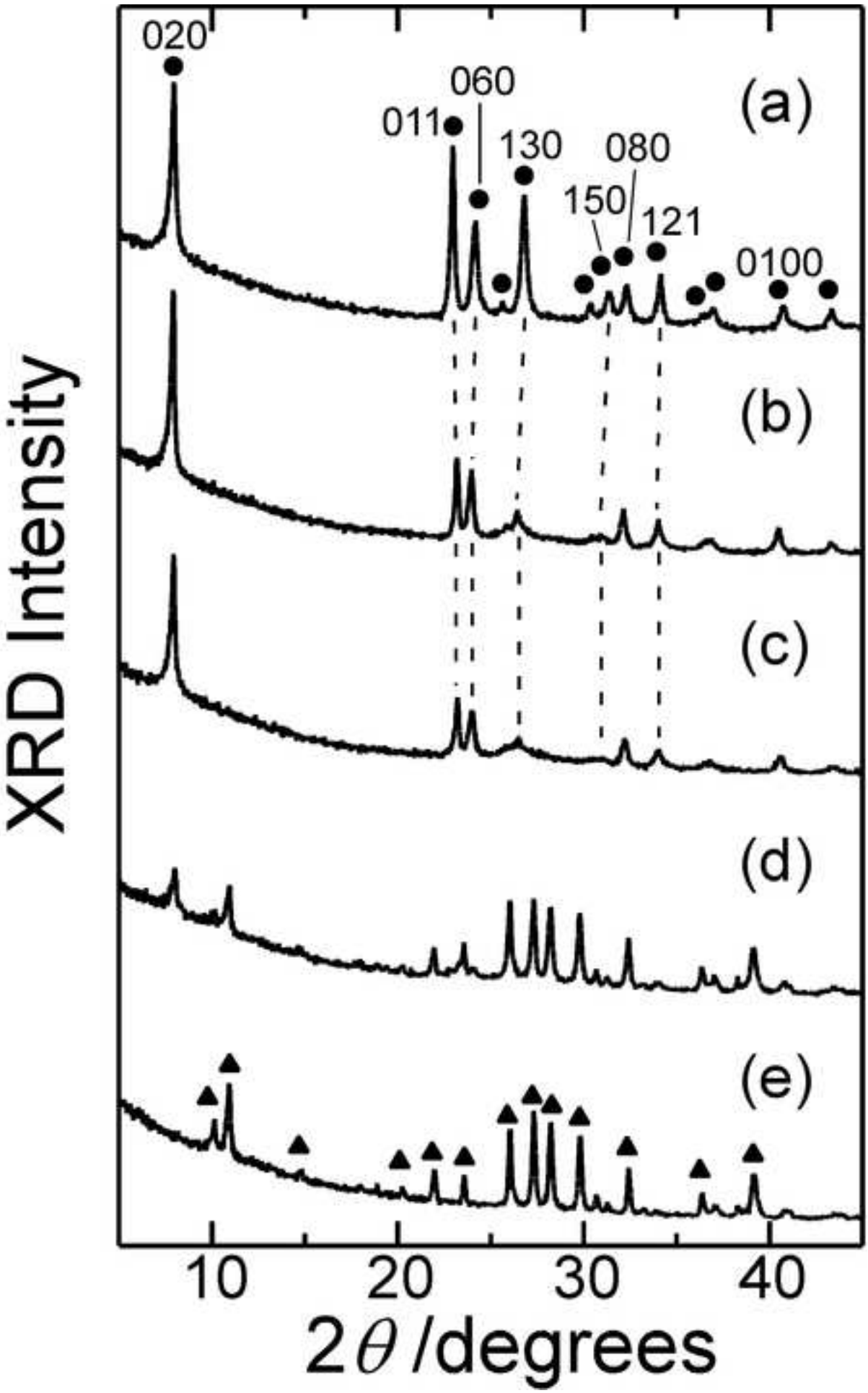
Click here to download Figure Figure 8.tif





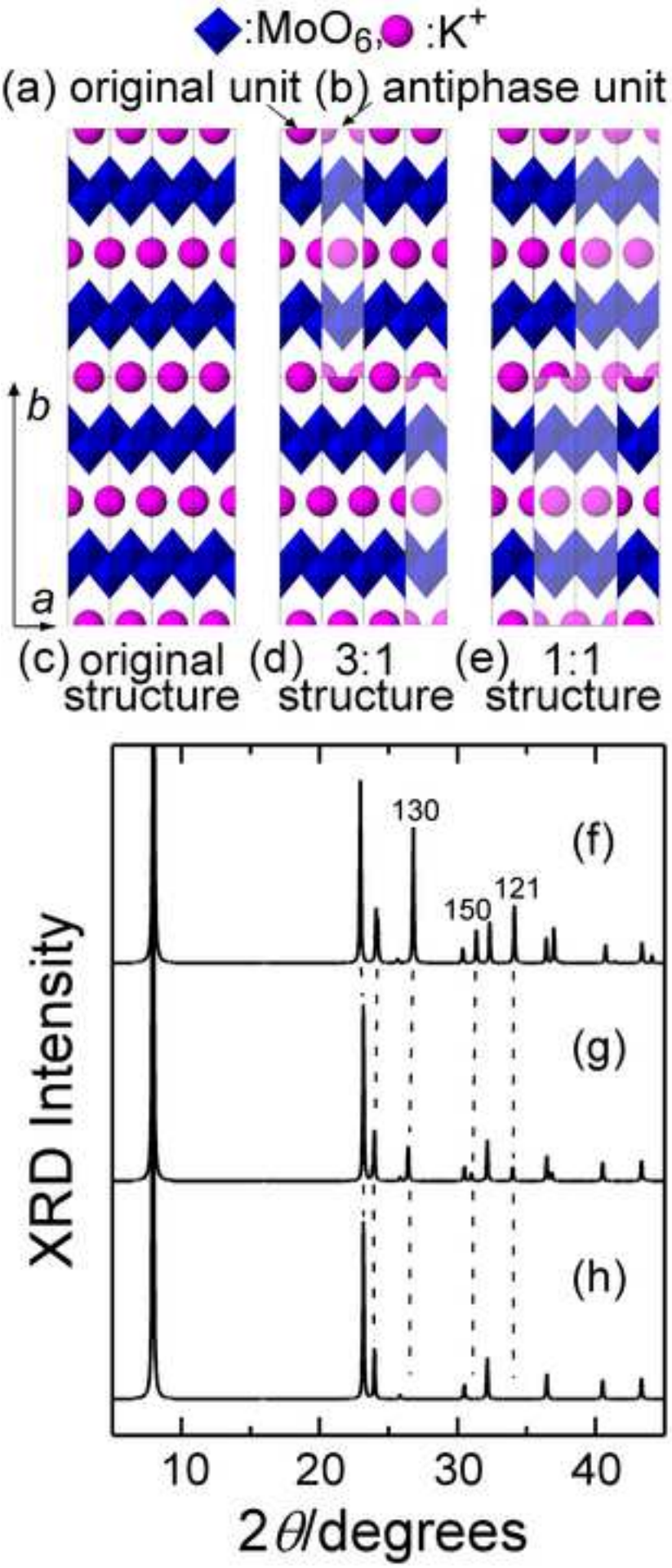
Figure

Click here to download Figure Figure 9 - XRD of HydKMB depending on time 100 x 60mm.tif



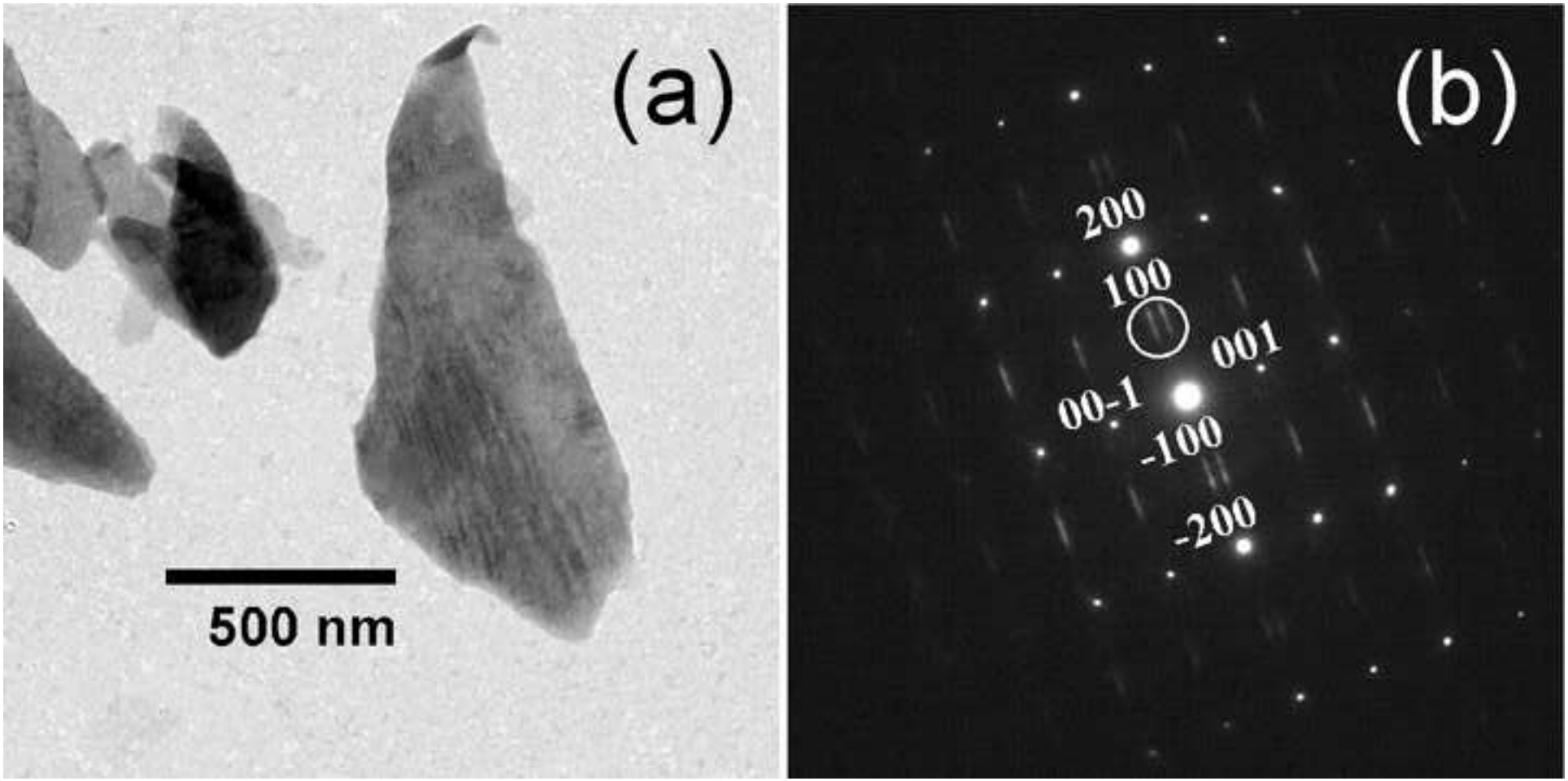
Figure

Click here to download Figure Figure 10New - 130 structures and XRD patterns.tif



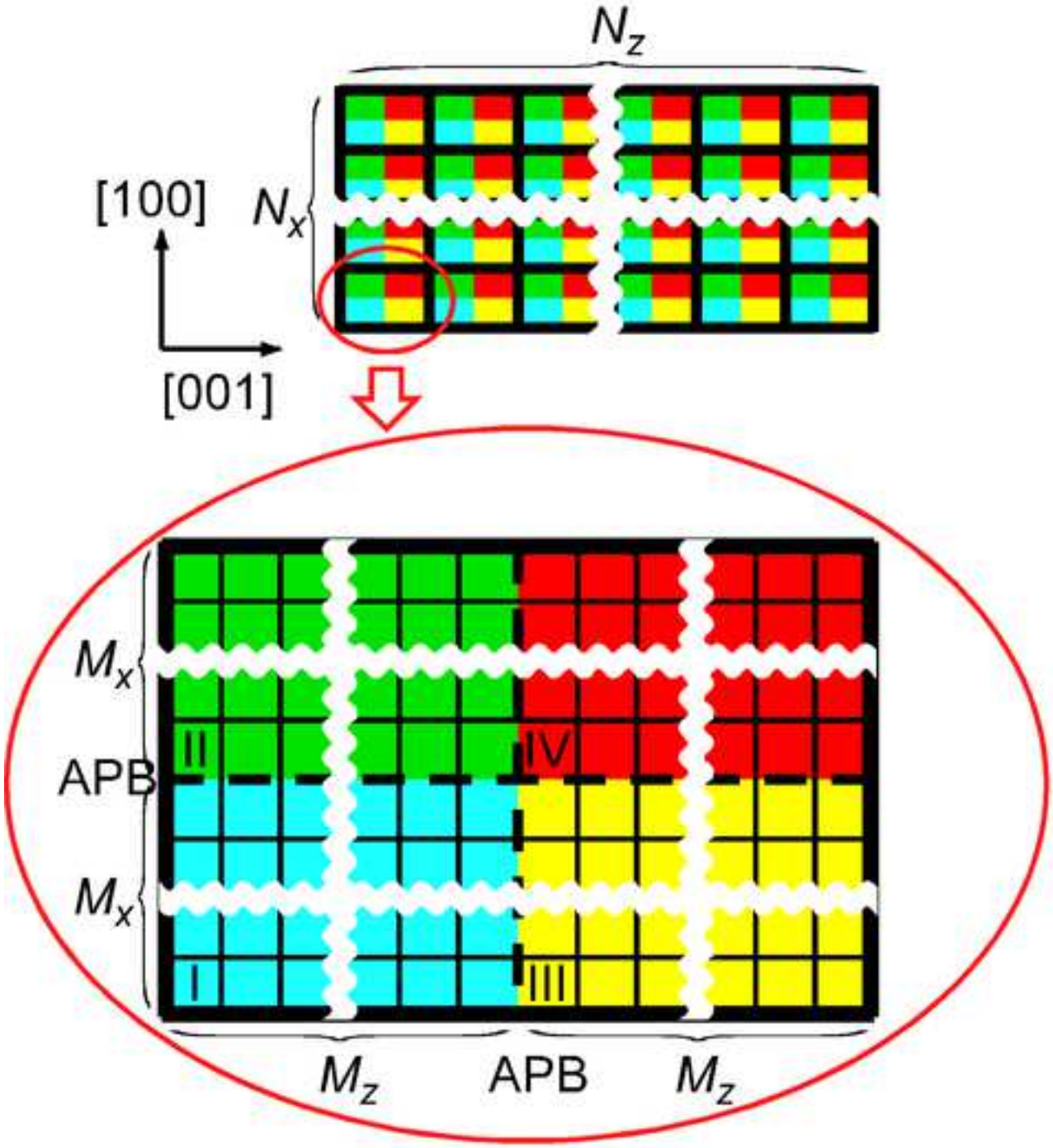
Figure

Click here to download Figure Figure 11 TEM SAED.tif



Figure

Click here to download Figure Figure 12 - 2DLRO Model1 100 x 70 mm.tif



– – : antiphase boundary (APB)

I : a unit corresponding to original unit cell of Hyd-K-MB

II : a unit antiphased along a certain direction

III : a unit antiphased along another direction

IV : a unit antiphased along the both directions

Figure

Click here to download Figure Figure 13 - 2DLRO Intensity.tif

